

H-band Quartz-Silicon Leaky-Wave Lens with Air-Bridge Interconnect to GaAs Front-End

Arias Campo, Maria; Holc, Katarzyna ; Weber, Rainer ; De Martino, Carmine; Spirito, Marco; Leuther, Arnulf ; Bruni, Simona; Llombart, Nuria

DOI

[10.1109/TTHZ.2021.3049640](https://doi.org/10.1109/TTHZ.2021.3049640)

Publication date

2021

Document Version

Accepted author manuscript

Published in

IEEE Transactions on Terahertz Science and Technology

Citation (APA)

Arias Campo, M., Holc, K., Weber, R., De Martino, C., Spirito, M., Leuther, A., Bruni, S., & Llombart, N. (2021). H-band Quartz-Silicon Leaky-Wave Lens with Air-Bridge Interconnect to GaAs Front-End. *IEEE Transactions on Terahertz Science and Technology*, 11(3), 297-309. Article 9316262. <https://doi.org/10.1109/TTHZ.2021.3049640>

Important note

To cite this publication, please use the final published version (if applicable). Please check the document version above.

Copyright

Other than for strictly personal use, it is not permitted to download, forward or distribute the text or part of it, without the consent of the author(s) and/or copyright holder(s), unless the work is under an open content license such as Creative Commons.

Takedown policy

Please contact us and provide details if you believe this document breaches copyrights. We will remove access to the work immediately and investigate your claim.

H-band Quartz-Silicon Leaky-Wave Lens with Air-Bridge Interconnect to GaAs Front-End

Marta Arias Campo, *Graduate Student Member, IEEE*, Katarzyna Holc, Rainer Weber, Carmine De Martino, *Graduate Student Member, IEEE*, Marco Spirito, *Member, IEEE*, Arnulf Leuther, Simona Bruni, and Nuria Llombart, *Fellow, IEEE*

Abstract—Thanks to the large bandwidth availability, millimeter and sub-millimeter wave systems are getting more attractive to be used in a wide range of applications, such as high-resolution radar or high-speed communications. In this contribution, a new lens antenna in-package solution is presented for the H-band (220–320 GHz), including a wideband quartz-cavity leaky-wave feed combined with an air-bridge chip interconnect technology, based on spray coating and laser lithography. This interconnection acts as a wideband, low-loss transition between the GaAs front-end and the quartz antenna, avoiding the use of expensive waveguide split-blocks. An antenna prototype including the interconnect has been manufactured and characterized, validating the full-wave simulated results for the integrated H-band leaky-wave with aperture efficiency higher than 74% over 34% bandwidth, and radiation efficiency higher than 70% over 37% of bandwidth.

Index Terms— mm-wave, H-band, lens antenna, leaky-wave antenna, air-bridge chip interconnect, off-chip antenna, antenna-in-package.

I. INTRODUCTION

THE development of integrated systems at mm- and sub-mm waves is leveraged by the growing interest in new applications requiring large bandwidth. Radar and communication are probably the most representative industries which promote and will profit from the emergence of the use of higher frequency bands [1]–[3]. The standardization of wireless communications at carrier frequencies in the 300 GHz band has already begun [4]. While allowing for larger bandwidths, the use of higher frequencies comes with increased propagation spreading loss and lower output power,

Manuscript received XXX; revised XXX; accepted XXX. Date of publication XXX; date of current version XXX. This work was supported in part by the German Federal Ministry of Education and Research (BMBF), within the project HYPATIA (ES2TECH019), and in part by the European Union through the ERC Starting Grant LAA-THz-CC under Grant 639749.

Marta Arias Campo is with IMST GmbH, 47475 Kamp-Lintfort, Germany, and was also with the THz Sensing Group, Delft University of Technology, 2628 CD Delft, The Netherlands (e-mail: arias@imst.de).

Katarzyna Holc, Arnulf Leuther and Rainer Weber are with Fraunhofer Institute for Applied Solid State Physics (IAF), 79108 Freiburg, Germany.

Carmine De Martino and Marco Spirito are with the Electronics Research Laboratory, Delft University of Technology, 2628 CD Delft, The Netherlands.

Simona Bruni is with IMST GmbH, 47475 Kamp-Lintfort, Germany.

Nuria Llombart is with the THz Sensing Group, Delft University of Technology, 2628 CD Delft, The Netherlands.

which can be compensated with high-gain and efficient antennas. Additionally, the efficiency in the transition between the antenna and the front-end becomes especially meaningful. The majority of systems operating in these frequencies make use of waveguide technology to interface between the front-end and antenna. Several chip to waveguide transitions have been proposed in the literature at H-band, presenting mostly losses higher than 1 dB [5]–[8]. In [9], a transition integrated in a GaAs chip with 0.5 dB loss was reported, reaching more than 100 GHz bandwidth. In any case, the manufacturing of mm-waveguide split blocks is very costly, and therefore they become unattractive for future commercial applications. Silicon micro-machined waveguides have been proposed as a more versatile and cost-efficient alternative [10]. However, the transmission from the chip to the waveguide remains a challenge, introducing additional losses.

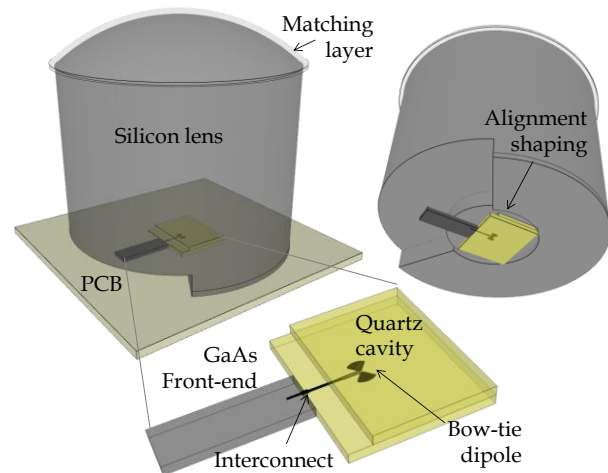


Fig. 1. Lens antenna concept with quartz leaky-wave feed and interconnect to GaAs front-end.

On-chip antennas have been already proposed as a more cost-effective and integrated approach. Solutions based on grounded patches with front-side radiation show increasing radiation efficiency for higher frequencies, but cover only a small bandwidth [11], [12]. Dielectric loaded on-chip antennas with front-side radiation [13]–[15] and end-fire radiation [16] have been proposed at 300 GHz, reaching high efficiencies but bandwidths lower than 13%. Antenna concepts based on radiation through the chip with silicon lenses have been proposed for imaging, radar or communication applications

[17]–[22], achieving large impedance bandwidths. In these back-radiating concepts, 1–1.5 dB losses occur due to the propagation through the lossy chip substrate. Antenna concepts such as double slots or dipoles are usually proposed, which do not reach high lens aperture efficiency over large bandwidths. In order to enable wideband, compact lens array concepts as discussed in [23], and coherent lens arrays as proposed in [24], high lens aperture efficiency is required over a large bandwidth, and therefore more complex lens feed designs are needed, such as leaky-wave (LW) feeds [25]. However, those are difficult to implement in on-chip approaches [18].

Off-chip antennas have been as well proposed at frequencies higher than 100 GHz for antenna-in-package (AiP) concepts, using e.g. Alumina [26], LTCC [27], Silicon membranes [28] or quartz carriers [29], achieving narrow bandwidths ($< 10\%$). In these concepts, MMIC area is spared and more degrees of freedom for the antenna design are introduced. Most of the concepts make use of bond-wires to connect the antenna with the active front-end MMIC, introducing loss and inductive effects which can be compensated with narrow-band matching networks. In [28], beam-leading technology is used at 150 GHz as an alternative to bond-wire transitions, enhancing the transition performance. A state-of-the-art compilation concerning 300 GHz on- and off-chip antenna solutions with front radiation was published in the recent work [29], reporting relative bandwidths lower than 15%.

In this work, a wideband antenna-in-package at H-band is proposed, shown in Fig. 1, employing the multi-layer quartz technology presented in [29] and exploiting leaky waves [25]. The use of quartz technology allows the development of more complex antenna concepts, thanks to the lower ohmic loss and the possibility to fabricate thicker and multiple substrate layers. Quartz Fabry-Pérot resonators [30], [31] and cavities [32] have been proposed in the literature at frequencies lower than 60 GHz, combined with metal-mesh mirrors and Frequency Selective Surfaces (FSS), respectively. However, the reported designs do not reach bandwidths higher than 10%. The integrated approach combined with a silicon lens proposed in this manuscript, enabling bandwidths larger than 30%, has not been reported to our knowledge. Quartz lenses have been reported with double-slot [33] and patch feeds [34], leading to higher back-radiation or reflection loss. Add-on quartz layers have been proposed for antenna-in-packaged array solutions, but lower efficiencies (45%) and narrow bandwidths ($< 10\%$) are reported [35], [36].

A new approach for the air-bridge interconnect technology is introduced in this work, achieving a low-loss, wideband connection from the antenna to the front-end chip, enabling the implementation of efficient off-chip antennas. The novel air-bridge interconnect technology, based on spray coating and laser lithography, achieves higher fabrication precision than [28]. The proposed technology introduces a considerable performance advantage with respect to bond-wire transitions (estimated transition loss lower than 0.2 dB over the whole H-band), and can be implemented with large-scale suitable

processes.

In order to cover the wideband high aperture efficiency requirement, a resonant LW antenna is proposed as lens feed. A similar antenna was presented in [23] using a plastic lens and air cavity fed by a split-block waveguide, reaching 80% aperture efficiency over more than 40% bandwidth. In this work, the LW feed is implemented in the multi-layer quartz technology presented in [29], using the novel air-bridge interconnect. The proposed LW antenna is composed of a quartz cavity and a silicon lens. The LW feed features high directivity inside the lens, enabling the use of a truncated lens with shallow shape [37]. The quartz LW cavity is excited by a dipole, enabling a wideband differential interconnection from the quartz to the front-end chip, with no need of ground connection. Moreover, the presented antenna-in-package concept allows mounting the front-end chips and implementing the transitions between them on top of a low-cost Printed Circuit Board (PCB) (e.g. FR4). The lens can be as well placed on top of the antenna quartz chip as a surface-mount component (Fig. 1), facilitating considerably its assembly.

A quartz LW antenna including an interconnect to a GaAs chip has been designed with minimized cavity size (integrated design). Full-wave simulations for this design show wideband impedance matching and stable patterns, reaching potentially more than 74% aperture efficiency over 34% relative bandwidth for an integrated prototype. Thanks to the low loss characteristic of both interconnect and transmission line on quartz, more than 70% radiation efficiency could be reached in the whole bandwidth with this integrated antenna. A prototype dedicated to the characterization has been fabricated, elongating the dipole transmission line to allow measuring the antenna with landing probes. Measurement results for this prototype are in very good agreement with full-wave (FW) simulations, validating the results for the integrated design.

The paper is organized as follows: Section II focuses on the LW feed concept; Section III presents the antenna-in-package technology, as well as the LW feed and lens analysis and design; Section IV describes the antenna prototype fabrication and characterization.

II. WIDEBAND LEAKY-WAVE ANTENNA

The proposed antenna geometry is sketched in Fig. 1. The quartz chip, which acts as lens feed, is placed beside the active front-end chip, and connected to it by means of the air-bridge interconnect technology presented here. The antenna consists of a resonant LW quartz cavity, comprised between a ground plane and the silicon lens, fed by a bow tie dipole. By choosing a dipole antenna as excitation of the LW cavity, we can benefit from the differential mode in the transition to the GaAs chip. The differential transition does not need any ground reference (hence no via connection), enabling wideband performance. Moreover, the chosen stack-up does not support the propagation of surface waves. In this section, the antenna concept is described more in detail. Besides, the fundamental differences between the LW excitation using a

slot or a dipole are briefly discussed.

A. Wideband Leaky-Wave Antenna Concept

Resonant LW or Fabry-Pérot antennas [38], [39], [25] exploit the propagation of a pair of LW modes, TM_1/TE_1 , along a half-wavelength dielectric cavity, in our case quartz (dielectric permittivity $\epsilon_r^c = 3.8$), placed between a ground plane and a dielectric material with higher dielectric permittivity ϵ_r , in our case the silicon lens ($\epsilon_r^l = 11.9$). While they propagate along the quartz cavity, the leaky-modes radiate energy into the silicon lens. In this way, the feed effective area increases, featuring more directive radiation patterns and improving the lens illumination efficiency. The feed directivity enhancement increases for a higher ϵ_r contrast between the cavity and lens material. This effect is linked to the critical angle in the interface between the cavity and the lens (34° for quartz-silicon), after which very low power is radiated by the LW antenna. The feed directivity improvement is however achieved at a cost of decreasing the antenna bandwidth [25]. The combination quartz-silicon presents a similar ϵ_r contrast to the one in concepts using a lens with low ϵ_r (~ 2.5) and an air cavity, where relative bandwidths larger 40% have been achieved [23]. The use of a silicon lens is advantageous in multi-beam architectures, as it enlarges the achieved field-of-view with respect to lenses with low ϵ_r [23], [33].

The LW cavity is fed by a dipole antenna, placed in its center (Fig. 1) and at half distance between the ground plane and the silicon (Fig. 2a). Having the cavity half-wavelength height, the distance from the dipole to the ground plane is quarter-wavelength, optimum for the wideband impedance matching of the dipole. Two layers of quartz, with equal height $h_c/2$, are stacked for this aim. A bow-tie dipole has been chosen to enhance the antenna impedance bandwidth.

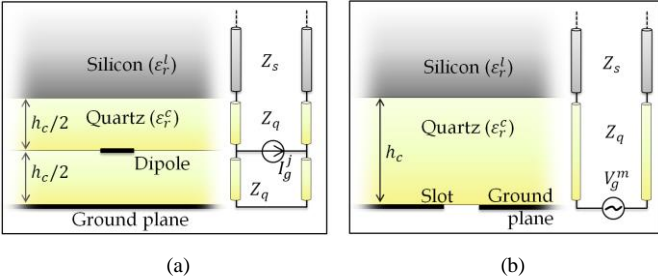


Fig. 2. Equivalent transmission line models for LW with quartz cavity and silicon semi-infinite media fed by a) dipole (used in this work) and b) slot. Metallic structures are drawn in black.

B. Leaky-Wave Source: Dipole vs. Slot

Resonant LW stratifications with a cavity between a ground plane and a denser semi-infinite media support an additional mode: TM_0 [40]. This TM_0 mode radiates at an angle close to the critical one, being likely to degrade the lens aperture efficiency, η_{ap} . Slot excitations have been usually applied in the literature to excite LW lens feeds (Fig. 2b), fed by squared waveguides [23], [25]. In this case, the effect of the TM_0 mode is very visible in the radiation pattern, and it is either cancelled [25] or attenuated [23] by means of a double-slot, in order to

keep high lens η_{ap} . The suppression of the TM_0 LW mode has been as well discussed in the literature for Fabry-Pérot antennas radiating in free-space [41]. In the antenna presented in this work, the dipole does not excite the TM_0 LW mode, which effect is therefore not visible in the radiation pattern.

The electric field radiated in the far-field by the same stratification, excited by an elementary magnetic source (infinitesimal dipole, Fig. 2a on the left) or by an elementary electric source (infinitesimal slot, Fig. 2a on the right), are compared in Fig. 3 for the E-plane. The radiation patterns are calculated with multi-layer Spectral Green's Functions (SGF) at the center frequency for $h_c = \lambda_d/2$ where λ_d is the wavelength in quartz. The contribution of both TM_0 and TM_1 leaky modes in the far-field has been separated for both excitations with the approach described in [42], which approximates the voltages and currents in the surrounding of the LW poles ($E_{TM_0}^{app}, E_{TM_1}^{app}$ in Fig. 3). The sum of the calculated contributions results in an approximated shape of the far-field, which has been as well plotted in Fig. 3 ($E_{TM_0+TM_1}^{app}$), normalized to broadside for the sake of comparison.

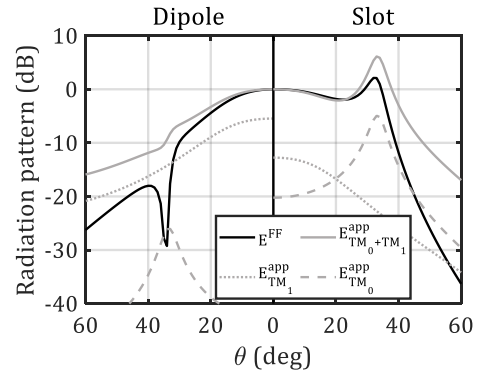


Fig. 3. E-plane radiation patterns normalized to broadside for the stratification shown in Fig. 2. Left: elementary electric source. Right: elementary magnetic source. Black: asymptotic calculation of the far-field with multi-layer Green's Function. Grey: far-field calculated with the potentials and currents approximated in the surrounding of the LW pole.

The contribution of the TM_1 mode is similar for both excitations, and represents well the fields in the surrounding of these poles. However, as it is clear in Fig. 3, the contribution of the TM_0 mode, which is strong and well represented by the approximation in case of the slot, is completely cancelled in case of the dipole. The dipole introduces a zero in the E-plane, inherent to the electric elementary source. In the case where the LW is radiating into a lens, $\epsilon_r^{FF} = \epsilon_r^l > \epsilon_r^c$, being ϵ_r^{FF} the permittivity of the medium where the far-field is calculated, the dipole zero is found in the critical angle between the cavity and lens, $\theta_{zero} = \sin^{-1}(\sqrt{\epsilon_r^c/\epsilon_r^l})$, [43]. Both the zero and TM_0 radiation angles are constant and almost coincident over a wide band, in which the contribution of the TM_0 to the far-field is consequently cancelled, as shown in Fig. 3 on the left.

Being the TM_0 mode contribution intrinsically cancelled by the dipole excitation, the geometry of this source does not need to be specifically optimized to shape the radiation

pattern. In this way, in contrast to the double slot, a single dipole may be used to excite the LW, and the dipole geometry may be optimized by only aiming for a wideband impedance matching.

The LW modes power attenuates inside the cavity along ρ as $e^{-2\alpha\rho}$, being with $\alpha = \text{Im}[k_\rho]$ [44], [45]. The TM_0 presents the smallest α , and it sets therefore the antenna effective area, when it propagates. For the stratification in Fig. 2, the TM_0 attenuation related to the mode radiation, $e^{-2\alpha\rho}$, reaches -10 dB at $\rho = 6\lambda_d$ over the whole bandwidth. If the TM_0 does not propagate, as with dipole excitation, the effective area is given by the TE_1 mode, hence significantly reduced. In this case, -10 dB attenuation is reached at a maximum $\rho = 1.4\lambda_d$ at 320 GHz. This smaller effective area allows truncating the LW cavity (here the quartz chip) at a much smaller size without affecting the radiation characteristic.

III. LEAKY-WAVE ANTENNA-IN-PACKAGE DESIGN

In this section, the stratification and geometry for the quartz chip, GaAs chip and interconnect used between them are explained in detail. The quartz LW feed and lens design methodology are as well described, and their final geometry and FW simulation results are shown for the design at H-band (220–320 GHz).

A. Antenna-in-Package Technology

The geometry and layer stack-up for the LW quartz feed, GaAs chip and interconnect are shown in Fig. 4. The top view shows the quartz chip, where the quartz top layer is transparent to show the dipole on the bottom layer. The top quartz layer is truncated at a length $sp = 300$ μm shorter than the bottom, in order to leave space to implement the interconnect to the GaAs chip. The dipole is manufactured on the bottom quartz layer, with a ground plane below. The antenna is realized in a 100 mm wafer technology using low loss fused silica substrates. The final wafer thickness is 135 μm with 3 μm thick plated Au layers on front and back side. The Au structures are defined using laser lithography and wet etching. Both quartz layers are bonded with a thin layer of thermoplastic glue (3 μm), which allows the two quartz chips to get in direct contact. The high precision alignment is performed manually, operating under a microscope, and facilitated thanks to alignment marks in both bottom and top quartz chips. This alignment process can be however automatized. It has been observed that an air gap remains between the glue and the outer side of the Au differential line strips, and no glue penetrates in the gap between both strips. This has been taken into consideration in the antenna design.

The GaAs MMIC and the quartz antenna are glued side-by-side using silver epoxy. The GaAs chip is manufactured with the same height as the bottom quartz chip, $h_c/2 = \lambda_d/4$, in order to allow for a flat interconnect, as it is shown in the side view. Alternatively, a preform may be placed below the GaAs chip in order to reach the desired height. In the detailed view of the stack-up, the metal and substrate layers in the GaAs are displayed. The differential line in the GaAs MMIC is

embedded in photo-benzocyclobutene material (PBCB). A ground plane shields the transmission line from the GaAs substrate.

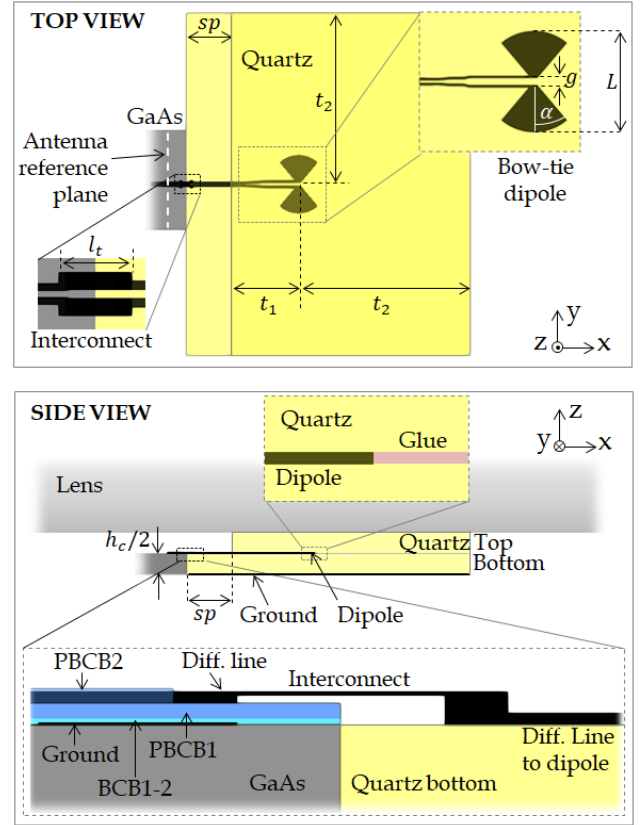


Fig. 4. LW feed geometry and stratification. Metallic structures (gold) are drawn in black. Top view: geometric parameters quartz chip: $sp = 300$ μm , $t_1 = 440$ μm , $t_2 = 1.13$ mm, $h_c = 270$ μm . Side view: 1) GaAs: gold thickness ground: 0.35 μm , differential line: 3 μm ; substrate thickness and ϵ_r : BCB1-2: 1.7 μm , $\epsilon_r = 2.7$, $\tan\delta = 0.002$, PBCB1: 3.5 μm , $\epsilon_r = 3.2$, $\tan\delta = 0.015$, PBCB2: 4 μm , $\epsilon_r = 3.2$, $\tan\delta = 0.015$. 2) Interconnect gold thickness: 0.8 μm . 3) Quartz: gold thickness: 3 μm , roughness: 0.08 μm ; glue: $\epsilon_r \sim 3$, 3 μm .

In order to implement the interconnect, the photo resist is spray coated over the chips and structured using high-resolution laser lithography to open the contact pads where the chip-to-antenna interconnect is to be placed. A metal stack layer is deposited by evaporating Ti/Au (30/500 nm, respectively) followed by the second lithography step, where the 20 μm wide interconnect metal stripes are defined. The length of the interconnect stripes, $l_t = 70$ μm , is tailored to match the distance between the chips. In the final step, the metal layer is etched away, leaving the defined chip-to-antenna interconnects. As a result, the metal stripes are running from the contact pads of the front-end GaAs chip over the supporting photoresist layer to the contact pad on the quartz bottom layer. After the final lift-off step, the photoresist is removed, leaving the air-bridge between the chips. In Fig. 5, the interconnect processing steps are shown with more detail. Fig. 6 shows a micrograph of a prototype realization of a GaAs-quartz interconnect, after the final metal etching step.

The loss in the air-bridge interconnect has been estimated by means of FW simulations, resulting less than 0.2 dB over

the whole frequency band. The loss in the differential transmission line in quartz has been measured as explained in the Appendix, going from 0.8 dB/mm at 220 GHz to 1.3 dB/mm at 320 GHz (Fig. 19).

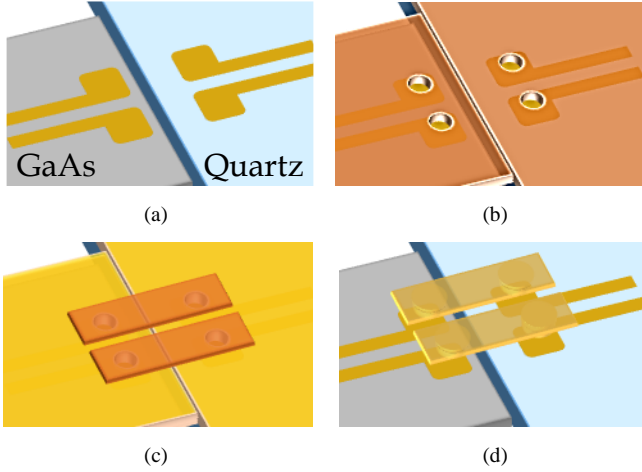


Fig. 5. Fabrication steps for an air-bridge interconnect between a GaAs MMIC (on the left) and a quartz chip (on the right). Yellow: gold. Orange: photoresist. Grey: GaAs. Blue: quartz. a) GaAs and quartz chips aligned. b) First lithography with vias fabrication. c) Metal stack deposited and second lithography. d) Metal etching and final lift-off.

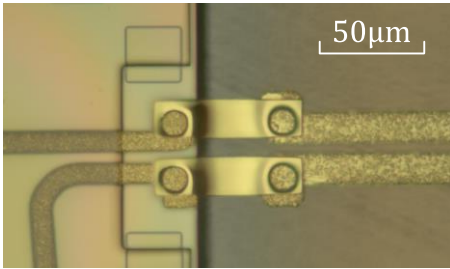


Fig. 6. Micrograph of a differential air-bridge interconnect between a GaAs MMIC (on the left) and a quartz chip (on the right).

B. Leaky-Wave Feed and Lens: Analysis and Design

As a first step in the LW antenna design, the LW feed radiation patterns inside the lens (primary patterns) have been estimated with an ideal dipole without transmission line, a non-truncated quartz cavity and the lens as a semi-infinite silicon medium. This can be modelled with SGF in multilayer stratified media, using the equivalent transmission line in Fig. 2a. A first optimization of the LW feed cavity height and phase center, and the lens truncation angle was carried out applying the analysis of the antenna in reception described in [23]. This analysis allows a fast optimization of the lens η_{ap} , including taper, phase, reflection and spill-over efficiencies. After this first evaluation, the cavity height was set to $h_c = 0.47\lambda_d$.

As a second step, the bow-tie dipole, placed at $z = h_c/2$, and transmission line were optimized by means of FW simulations with EMPIRE XPU [46] to maximize the impedance bandwidth. The dipole geometry parameters were set to $L = 0.66\lambda_d$, $\alpha = 40^\circ$ and $g = 28 \mu\text{m}$ (Fig. 4), providing a wideband matching to a 150Ω differential line. In

the GaAs front-end, 100Ω differential impedance is provided ($8 \mu\text{m}$ width and $8 \mu\text{m}$ gap). The dipole feeding line has been tapered in two steps to transform 150Ω into 100Ω differential impedance. In the region where no top quartz layer is present, the differential line parameters were adapted to preserve the 100Ω differential impedance. Initially, a benzocyclobutene (BCB) layer was planned to cover this piece of transmission line, which was dimensioned with $10 \mu\text{m}$ width and $10 \mu\text{m}$ gap to provide 100Ω . This BCB layer was finally not used, becoming the impedance here 125Ω . The small impact of this mismatch is included in the simulations. The interconnect is implemented with two stripes with $20 \mu\text{m}$ width and $10 \mu\text{m}$ gap (Fig. 6). This does not affect significantly the matching, since the impedance variation is less than 15% and the interconnect is short in terms of wavelength ($l_t = 0.06\lambda_0$). The FW scattering parameters (S-parameters) for the AiP at the reference plane (Fig. 4 top view) are shown in Fig. 7a.

After fixing the dipole and line geometry, the analysis in reception was applied to the primary patterns obtained from FW simulations with semi-infinite silicon medium and non-truncated quartz cavity. The goal was to fine tune the lens truncation angle and feed phase center in order to maximize η_{ap} over the whole bandwidth. A silicon lens with 8mm diameter has been considered, for which the optimum ellipse truncation angle is 30° , and the feed phase center $0.64\lambda_d$ below the ground plane.

Finally, the truncation size of the quartz cavity was optimized. The truncation length on the differential line side (H-plane) should minimize the transmission line loss, while preserving the primary patterns and impedance matching. The cavity truncation on this side can be performed at $t_1 = 0.75\lambda_d$ distance from the dipole at the centre frequency, where the TE_1 mode attenuation due to the radiation reaches -10 dB at 270 GHz, and -6.5 dB at 320 GHz. Applying the analysis in reception to the FW primary patterns including the truncated cavity, it has been estimated that the antenna η_{ap} is degraded in less than 0.1 dB at 320 GHz with this truncation. This is also partly thanks to the additional, length $sp = 0.64\lambda_d$ needed on the bottom quartz layer for the implementation of the interconnect (Fig. 4), which enlarges the effective truncation length. The resulting transmission line length is $730 \mu\text{m}$, with a maximum estimated loss of 0.9 dB at 320 GHz. The opposite side and perpendicular with respect to the transmission line may be truncated at a larger dimension ($t_2 = 1.13 \text{ mm}$), in order to mechanically support the silicon lens, which lies on the quartz chip (Fig. 4).

The FW primary patterns including the truncated quartz cavity, bow-tie dipole, differential line and interconnect (AiP), are shown in Fig. 7b at the center frequency. This figure displays as well as a reference the primary patterns calculated for an ideal dipole with the same length L , without cavity truncation or transmission line. Fig. 7a displays the directivity at broadside over the whole frequency band for both cases, with a maximum directivity variation of 2 dB over frequency. The AiP results are still in good agreement with the ideal dipole after including all the non-ideal effects. The most

significant difference is the cross-polar level, which increases in the AiP, due to the transmission line radiation.

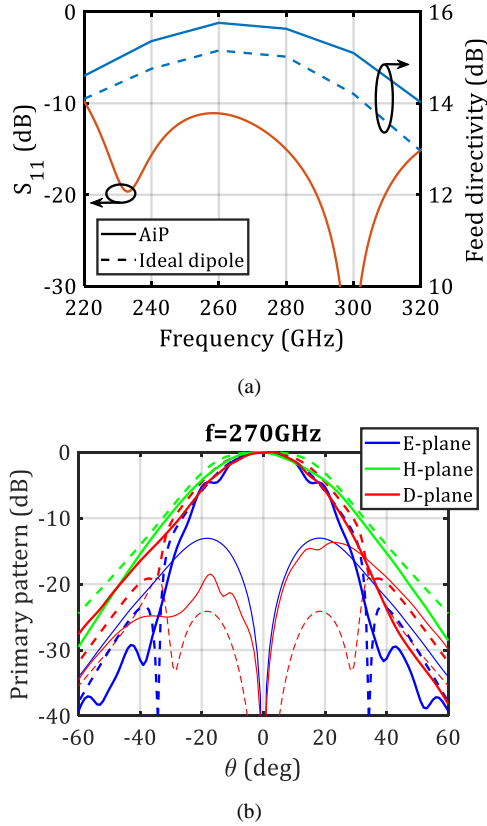


Fig. 7. a) Left axis: reflection coefficient of LW feed with $730\mu\text{m}$ long feeding line, with the silicon lens modelled as semi-infinite medium. The reference impedance is 100Ω differential, taken at the GaAs chip in the reference plane shown in Fig. 4. Right axis: Feed directivity over frequency inside the lens at broadside (lens modelled as semi-infinite medium). AiP: FW simulations including the truncated quartz cavity, bow-tie dipole, $730\mu\text{m}$ differential line and interconnect. Ideal dipole: SGF model with ideal thin dipole. b) Feed radiation patterns at the center frequency. Solid lines: AiP FW simulations; dashed lines: ideal dipole SGF simulations. Thick lines: co-polar. Thin lines: cross-polar.

The lens radiation patterns have been calculated for the ideal dipole applying Physical Optics (PO), as well as for the complete AiP FW model in EMPIRE XPU with multiple reflections, including the truncated quartz cavity, bow-tie dipole, differential line and interconnect (Fig. 8a). A standard $\lambda/4$ matching layer with $\epsilon_r = 2.8$ has been considered in both simulations. The matching layer ϵ_r corresponds to SUEX material [47], which later on will be used in the fabrication. The cross-polar level increase in the AiP due to the feeding line radiation is also visible in the lens patterns. Fig. 8b shows the FW simulated maximum directivity and gain for the AiP with the lens. The gain includes losses in the interconnect (<0.2 dB), differential line (<0.9 dB), and lens (<0.4 dB). The loss from the differential line is estimated via measurements as described in the Appendix. The η_{ap} (defined as the ratio between the directivity obtained with the lens, and the maximum directivity possible for this circular aperture) estimated with FW simulations for the AiP and the analysis in reception (FW-Rx), validated with FW simulations including

the lens multiple reflections, is higher than 74% over 34% bandwidth, as shown in Fig. 9. The AiP efficiency decay at the higher part of the band with respect to the ideal dipole is related to phase and polarization loss introduced by the feeding line. The power lost in cross-polar is always lower than 0.5 dB. The overall AiP radiation efficiency, η_{rad} , (ohmic and dielectric losses) is higher than 70% over the whole frequency band, as also displayed in Fig. 9.

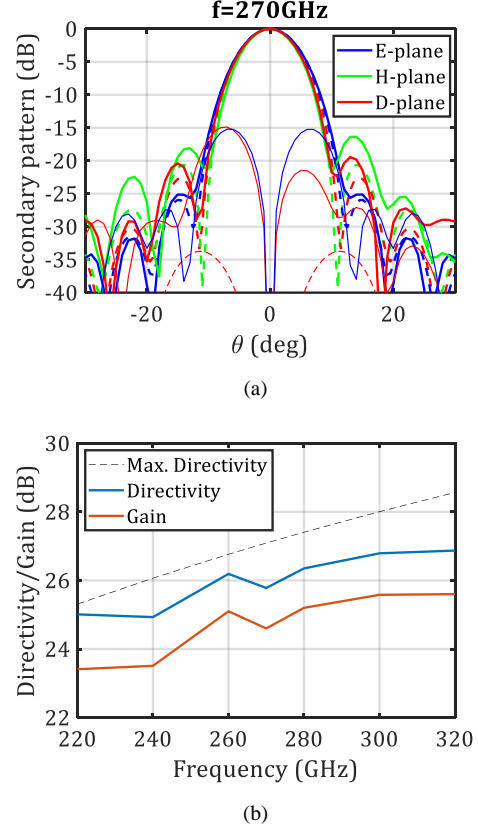


Fig. 8. a) Lens radiation patterns at the center frequency. Solid lines: AiP with lens, FW simulations with multiple reflections. Dashed lines: ideal dipole, PO simulations. Thick lines: co-polar. Thin lines: cross-polar. b) FW simulated maximum directivity and gain over frequency for the AiP with lens. The maximum directivity for the equivalent circular aperture has been plotted as reference in dashed black line. The FW simulation with multiple reflections includes the interconnect, feeding line, truncated cavity and lens with matching layer.

C. Antenna Self-Coupling

A good estimation of the lens aperture and radiation efficiency can be obtained by calculating the power coupled back in the feed when placing a flat metallic reflector on top of the lens, in the near-field (Fig. 10a). This is equivalent to computing the power coupled between mirrored lenses (image theory), as performed in [23], which facilitates the gain estimation of this kind of lens antenna. The field is collimated by the lens and features a planar phase front in this near-field region, thanks to the antenna high aperture efficiency. Therefore, the incident field in the metal reflector, \vec{E}_{tx} , can be estimated through geometrical optics (GO) propagation, with the expression in [23], under the assumption that all rays propagate in z-direction after the lens (Fig. 10a). The antenna

self-coupling efficiency, η_c , can be calculated applying the analysis in reception explained in [48] as

$$\eta_c \approx \frac{\left| \int_0^{2\pi} \int_0^{\frac{D}{2}} \vec{E}_{tx}(\rho, \phi) \cdot \vec{E}_{rx}(\rho, \phi) \rho d\rho d\phi \right|^2}{4\zeta_0^2 P_{rad}^2} \quad (1)$$

being ζ_0 the wave impedance in vacuum, D the lens diameter, $\vec{E}_{rx} = -\vec{E}_{tx}$ the field reflected in the metal plate and P_{rad} the power radiated by the LW feed. Note that η_c corresponds to the spill-over, reflection, phase, polarization and radiation efficiencies related to two identical antennas, as

$$\eta_c = (\eta_{so}\eta_{ref}\eta_{ph}\eta_{poi}\eta_{rad})^2 = \left(\frac{\eta_{ap}}{\eta_{tap}} \eta_{rad} \right)^2 \quad (2)$$

where η_{tap}^{amp} is the amplitude taper efficiency, being this the only term in η_{ap} which does not come in to play in the coupling.

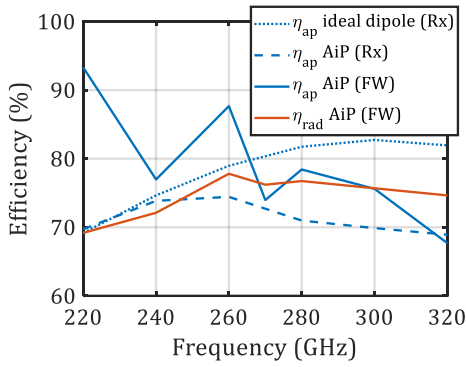


Fig. 9. Lens aperture efficiency and radiation efficiency (dielectric and ohmic loss). Ideal dipole Rx: analysis in reception applied to the primary patterns for an ideal dipole. AiP Rx: analysis in reception applied to the FW simulated primary patterns for the AiP with interconnect, feeding line and truncated cavity. AiP FW: simulation with multiple reflections for the AiP including interconnect, feeding line, truncated cavity and lens with matching layer.

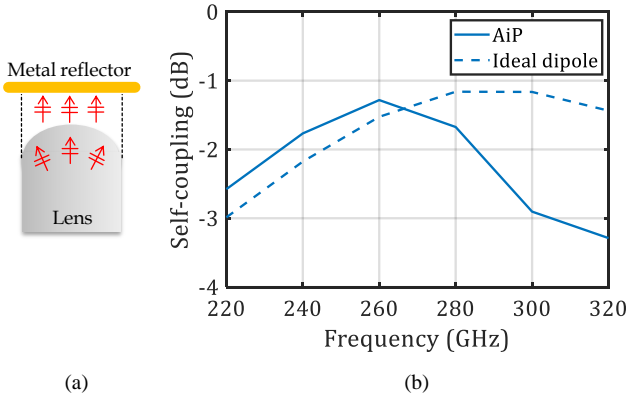


Fig. 10. a) Conceptual representation of the self-reflection setup. b) Lens self-coupling (no dielectric or ohmic loss) evaluated with the analysis in reception. Ideal dipole: analysis in reception applied with the primary patterns for an ideal dipole. AiP: analysis in reception applied with the FW simulated primary patterns for the dipole with interconnect, feeding line and truncated cavity.

Applying this analysis in reception, η_c has been calculated for the ideal dipole and infinite quartz cavity, as well as for the FW simulated AiP with truncated cavity, bow-tie dipole,

feeding line and interconnect, radiating in a semi-infinite silicon medium, as shown in Fig. 10b. For the sake of comparison, no dielectric or ohmic losses (η_{rad}) have been considered in the AiP calculation. The difference between the AiP η_c and the ideal dipole corresponds to additional phase and polarization loss introduced by the dipole feeding line, as previously mentioned. As the transmission line dimensions are larger in terms of wavelength for the higher frequencies, its radiation becomes increasingly significant in that case.

IV. ANTENNA PROTOTYPE AND MEASUREMENTS

In this section, the prototype fabricated to validate the integrated antenna performance shown in Section III.B is described, containing a longer transmission line to enable measurements with landing probes. The measurements performed to validate the antenna matching, radiation patterns and gain, are as well explained. The one-port S-parameters and coupling measurements are calibrated with the SOL (Short-Open-Load) method until the probe landing pads by means of Quartz calibration wafers [49].

A. Antenna Prototype

In order to enable the characterization of the lens antenna, a longer quartz chip dedicated to the measurements was manufactured, with a feeding line length of 6.4 mm, allowing contacting the antenna with the probes from the top side (Fig. 11a and Fig. 11d). The fabricated quartz antenna is connected with the novel interconnect to the GaAs chip which later will contain the front-end. A delay-line balun in the GaAs chip enables the antenna characterization with single-ended WR3 landing probes (Fig. 11b). The delay-line balun is implemented in the GaAs stratification shown in Fig. 4, and its characterization is shown in the Appendix. Fig. 11c shows a detail of the fabricated dipole embedded between the two quartz chips, where the mentioned air gap between the glue and the gold structures can be appreciated.

A silicon lens has been fabricated with diamond turning. On the bottom side of the lens, a circular profile with diameter equaling the diagonal dimension of the quartz chip enables an accurate alignment between the dipole and the lens focus (Fig. 1). A deeper opening was realized with laser cut on the side where the antenna is connected to the active front-end, in order to leave space for the rest of front-end chips and surface mount components, as shown in Fig. 1. The accuracy in this opening is not critical, as the LW lens feed does not illuminate the lens bottom area. After all front-end chips have been mounted on the PCB, the lens can be placed on top without the need of a microscope, allowing to speed up the fabrication process.

The lens has been provided with a matching layer realized with 165 μm thick SUEX coating, following the procedure described in [47]. As shown in Fig. 11a, only the top part of the lens has been covered, as very low energy is present in the lateral lens area, thanks to the directive LW feed radiation patterns inside the lens. This facilitates considerably the matching layer implementation.

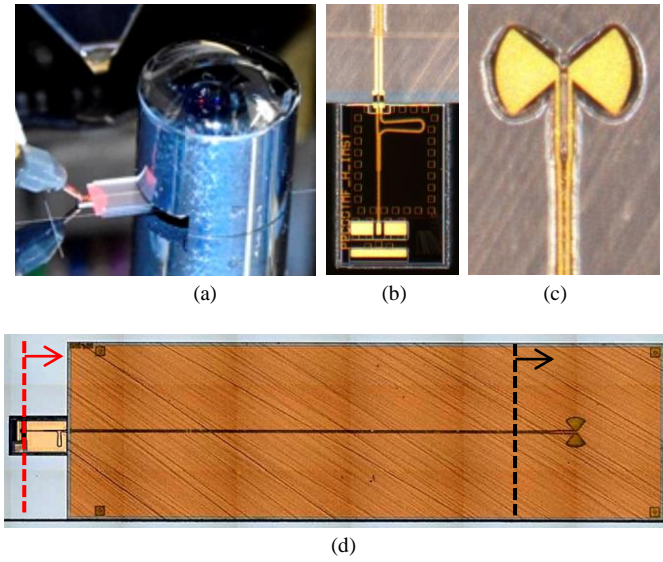


Fig. 11. a) Silicon lens with longer quartz feed (6.4mm transmission line) for S-parameter and near-field characterization. b) GaAs delay-line balun connected to the antenna feeding line in the quartz chip. c) Micrograph of the fabricated dipole. d) Full view of the long quartz antenna fabricated for characterization purposes, with GaAs balun on the left. The red dashed line marks the measurement reference plane. The black dashed line marks the size of the antenna to be integrated in the final system (Fig. 4).

B. Antenna Scattering Parameters

The measured antenna matching is shown in Fig. 12a, for a lens with matching layer, compared to FW simulations with the same antenna geometry (6.4 mm transmission line length), including the interconnect and GaAs delay-line balun (reference plane shown in Fig. 11d). Both results show good agreement. Fig. 12b shows the measured antenna S_{11} in time domain. Here, reflections from the different interfaces in the design have been identified. The S_{11} for a lens without and with matching layer are compared, showing the reduction in the first reflection coming from the lens interface in case of using matching layer. The result of time-gating the reflection corresponding to the dipole is as well displayed in Fig. 12a. The level of the time-gated reflection in the dipole is as well in good agreement in FW simulations and measurements. This is a second validation of the accurate loss estimation with the transmission line on the quartz chip done in the Appendix.

C. Far-Field Measurements

The characterization of the lens antenna far-field was performed by measuring the near-field on top of the lens with an open ended WR3 waveguide probe, as shown in Fig. 13a. An area of $22 \times 22 \text{ mm}^2$ was scanned with steps of $440 \mu\text{m}$ at 1.5 cm distance of the lens equivalent aperture. Both co- and cross-polar near-fields have been measured over the same plane and area, introducing a twist to rotate the waveguide probe polarization in case of the co-polar measurement. The resulting far-field patterns are shown in Fig. 14, compared to the ones estimated with FW simulations, showing good agreement. The loss introduced by the twist, estimated to be 1 dB, has been calibrated in the co-polar measurement. A beam steering of 3° was observed in the radiation patterns,

corresponding to $-120 \mu\text{m}$ feed shift in x-direction (reference system in Fig. 4). The measured radiation patterns have been centered in Fig. 14 for the sake of comparison. Fig. 15a shows the measured and FW simulated directivity over frequency, in good agreement. The measured co-polar directivity has been normalized to the power measured for both co- and cross-polar components, as it is the case in the FW simulation. Fig. 15b compares the measured and FW simulated polarization loss, calculated as the ratio between the co-polar power and the total radiated power, showing in good agreement. The polarization loss increases in the higher part of the band, due to the common mode excited by the non-ideal balun, and the longer transmission line length used in this prototype dedicated to characterization. A FW simulation substituting the balun by an ideal differential excitation shows cross-polarization loss lower than 0.5 dB (Fig. 15b).

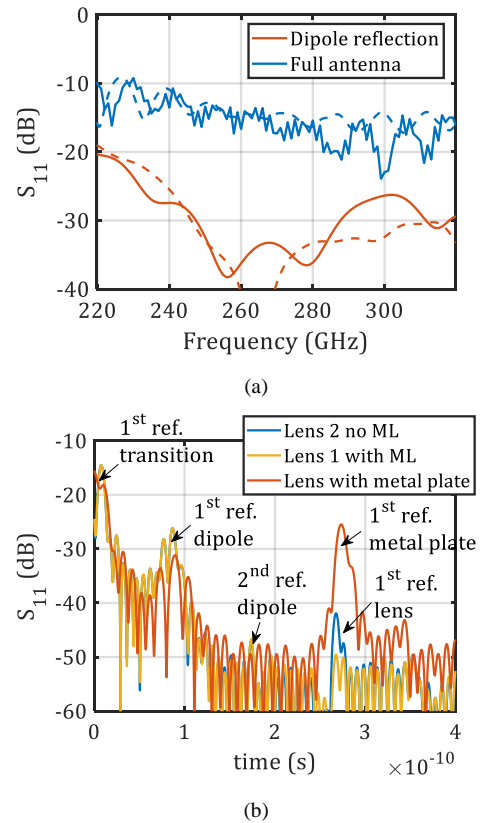


Fig. 12. a) Antenna reflection coefficient for the prototype in Fig. 11, at the marked reference plane. Dashed: FW simulations. Solid: measurements. The FW simulated S_{11} does not include the effect of multiple reflections in the lens. In both FW and measurements, the dipole reflection is calculated applying a time window from 0.05 ns to 0.12 ns. b) Antenna reflection coefficient measurements in time-domain, for lenses with and without matching layer (ML), and for the self-coupling setup. The reflections in the different interfaces have been marked, indicating the reflection order.

D. Antenna Gain: Self-Coupling Measurement

In order to validate the simulated antenna gain, the power coupled from the reflection from a metal plate on top of the lens has been measured. The measurement setup is shown in Fig. 13b, where the metallic reflector is placed at $500 \mu\text{m}$ distance from the lens equivalent aperture. Using this setup,

only one-port needs to be calibrated. Moreover, as shown in (2), this measurement setup is proportional to η_{rad}^2 , simplifying the antenna efficiency measurements. The antenna efficiency terms contributing to the self-coupling were explained in Section III.C. Here, the reference plane is located as shown in Fig. 11d, and therefore the coupling includes the loss in the delay-line balun and long feeding line. Fig. 12b shows the measured S_{11} in time domain, where the reflection coming from the metallic reflector has been identified. A FW simulation, including dielectric and ohmic loss, reproducing the measurement setup has been performed, using a perfect electric conductor as reflector. The $-120\ \mu\text{m}$ estimated off-focus displacement of the feed has been included in the FW simulation, in order to consider the corresponding phase loss coming from the plate reflection. The results, time-gated to evaluate the reflection coming from the metallic reflector, are shown over frequency in Fig. 16 for both FW simulation and measured results, showing good agreement. The differences between FW and measurement results are related to the tolerances in the measurements, dielectric and ohmic losses modelling, and prototype fabrication (balun, interconnect, quartz antenna, silicon lens and matching layer).

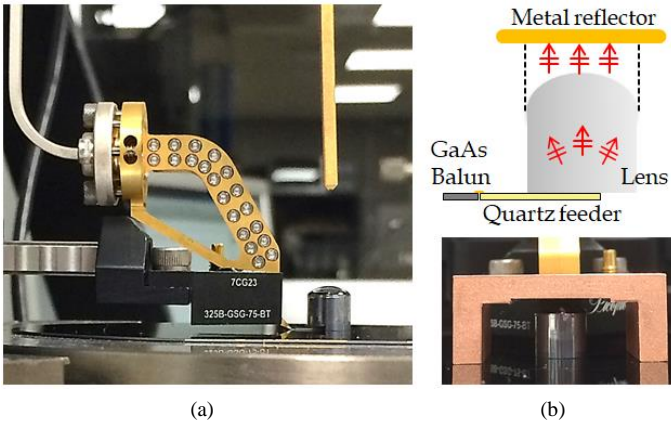


Fig. 13. a) Near-field measurement setup. b) Measurement setup for self-coupling. Top: sketch of the prototype and reflector. Bottom: photo of the setup, showing the lens and copper bridge acting as reflector.

Table I shows a summary of the different loss contributions in the antenna with short transmission line ($730\ \mu\text{m}$) for the integrated front-end, and the antenna with long transmission line ($6.4\ \text{mm}$) for characterization purposes. Those have been validated by means of the self-coupling measurement, together with the near-field and feeding line characterization.

TABLE I
ANTENNA LOSS CONTRIBUTIONS

Feeding line (μm)	Freq. (GHz)	Balun (dB)	Inter-connect (dB)	Feeding line (dB)	Lens & ML (dB)	Polarization (dB)
730	220	1.3	0.2	0.6	0.4	0.0
	320	1.6	0.2	0.9	0.4	0.3
6400	220	1.3	0.2	5.1	0.4	0.4
	320	1.6	0.2	8.3	0.4	1.8

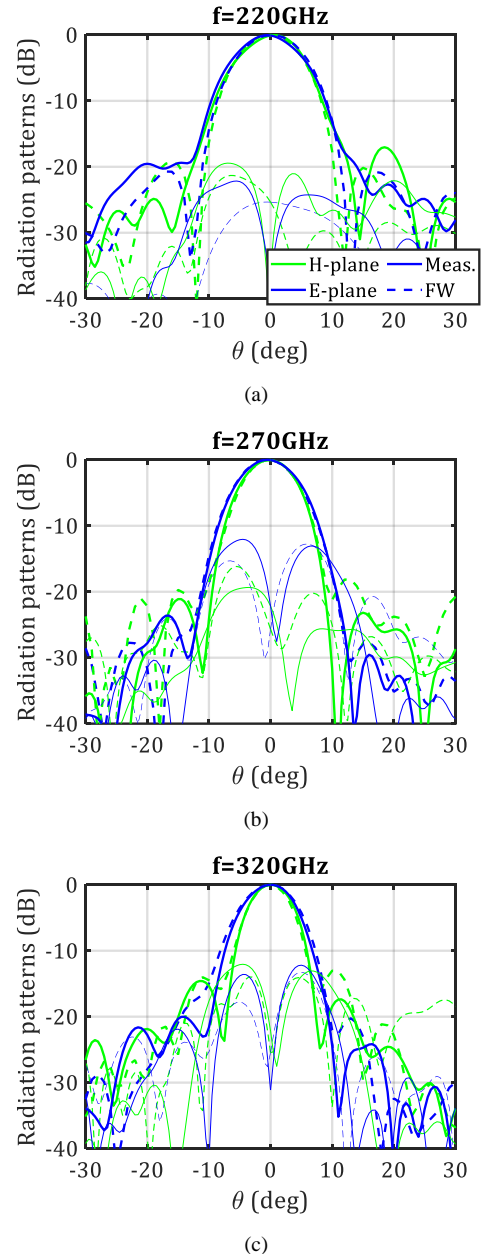


Fig. 14. Lens far-field patterns for the prototype in Fig. 11. Thick line: co-polar. Thin line: cross-polar. a) 220 GHz, b) 270 GHz, c) 320 GHz.

V. CONCLUSION

In this contribution, a wideband H-band leaky-wave antenna with a quartz cavity fed by a dipole is presented, to be used as silicon lens feed. The quartz antenna is connected to the active GaAs front-end by means of a novel air-bridge interconnect technology based on spray coating and laser lithography. The new proposed packaging approach avoids the use of waveguide split-blocks, and facilitates the front-end assembly. The combination of this packaging with the proposed leaky-wave feed configuration leads to an appealing integrated antenna solution for this band. Full-wave antenna simulations show good impedance matching, aperture efficiency higher than 74% over 34% bandwidth, and radiation efficiency higher than 70% over 37% bandwidth for an

integrated antenna. The radiation efficiency accounts for losses in the GaAs-quartz interconnect, dipole feeding line and lens. A prototype dedicated to the characterization has been fabricated. Scattering parameters, near-field and coupling measurement have been performed, validating the performance of the proposed integrated antenna-in-package solution at H-band.

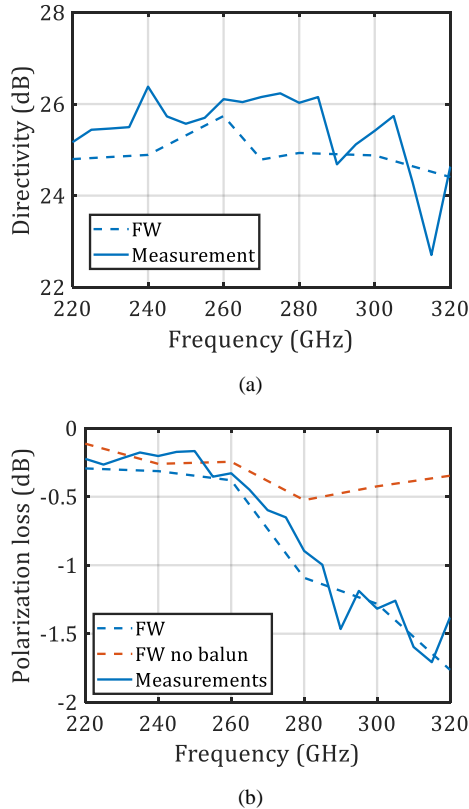


Fig. 15. a) Lens antenna directivity and b) lens antenna polarization loss (ratio between power radiated in co-polar and total radiated power). All curves correspond to the long antenna prototype dedicated to the characterization (reference plane shown in Fig. 11d). The FW simulation without balun in b) is performed substituting the balun with a differential port.

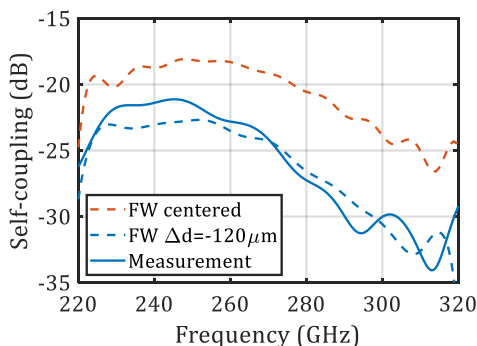


Fig. 16. Time-gated S_{11} of the lens antenna with a metallic reflector placed at $500 \mu\text{m}$ from the lens top (measurement setup in Fig. 13b). The time domain signal is shown in Fig. 12b. A window from 0.23 ns to 0.32 ns has been applied, to account only for the first reflected wave.

APPENDIX

In this appendix, the validation of the estimated losses in the interconnect between the quartz and GaAs chip, the quartz differential transmission line feeding the dipole, and baluns used for the characterization, is described. In order to enable the use of single-ended WR3 landing probes, baluns implemented in the GaAs MMICs have been included in all measurements to transform the differential mode into single-ended. The delay-balun used in the antenna measurements has been as well characterized, in order to de-embed its contribution. The two-port S-parameters measurements have been calibrated until the probe landing pads with the TRL (Through-Reflect-Line) method on a commercial impedance standard substrate (ISS).

A. Feeding Line and Interconnect Characterization

The losses in the differential transmission line in quartz were characterized by measuring 1) a back-to-back structure with two rat-race baluns (Fig. 17a), and 2) the same baluns with a quartz differential transmission line in between (Fig. 17c), connected with air-bridge interconnects. The 2.75 mm long transmission line is implemented in the same quartz stratification with bottom and top layers where the antenna is embedded, shown in Fig. 4. The differential line has the same impedance as will later be used in the antenna transmission line (100Ω). The rat-race balun was designed in the GaAs MMIC with the stratification shown in Fig. 4. The balun provides a single-ended input impedance of 50Ω and transfers this to 100Ω differential impedance.

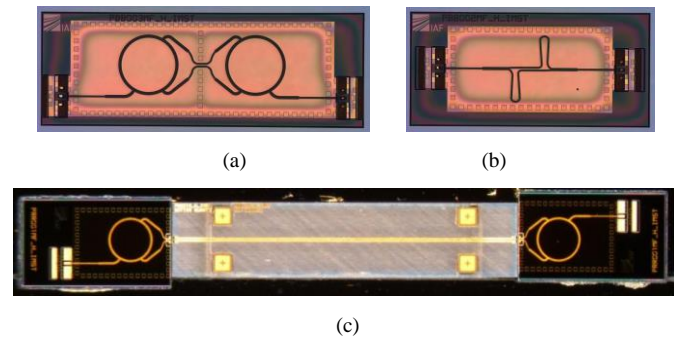


Fig. 17. Fabricated back-to-back structures a) Rat-race baluns for interconnect and quartz differential transmission line characterization. b) Delay-line baluns used in the antenna characterization. c) Rat-race baluns with 2.75mm long quartz transmission line (two interconnects).

Fig. 18 shows the FW simulated and measured S-parameters for both back-to-back structures, with good agreement over the whole frequency band (average error 1 dB). Note that FW simulations do not include the effect of the landing pads, which originate the mentioned difference with the measured results. Fig. 19 displays the transmission for the 2.75 mm differential line and two interconnects, calculated as the ratio between the S_{21} measurements for the back-to-back structures in Fig. 17a and Fig. 17c. By applying this ratio, the effect of the landing pads is mostly compensated. The results are compared with the ones estimated from FW simulations, showing good agreement. Taking into account 0.2 dB loss for

a single interconnect, estimated with FW simulations, the calculated loss in the differential transmission line in quartz goes from 0.8 dB/mm at 220 GHz to 1.3 dB/mm at 320 GHz (Fig. 19).

B. Delay-Line Balun for Antenna Measurements

The delay-line balun loss was validated with measurements by means of a back-to-back structure, shown in Fig. 17b, showing good agreement with FW simulations (Fig. 20). The effect of the landing pads is comparable to the one observed in Fig. 18.

ACKNOWLEDGMENT

The authors would like to thank Alexandra Serwa and Dr. Peter Uhlig from IMST GmbH Technology group for the matching layer implementation and for supporting us with measurements to verify the lens mechanical accuracy, as well as Roger Lozar from Fraunhofer IAF for H-band S-parameter characterization.

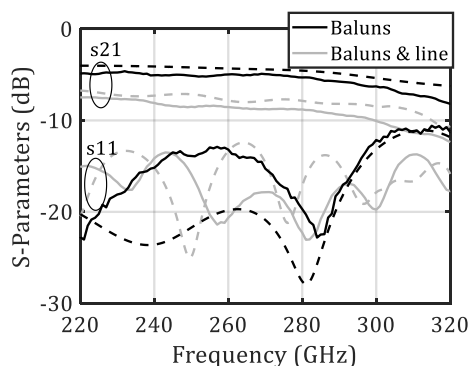


Fig. 18. S-parameters for the back-to-back rat race balun (Fig. 17a) and back-to-back rate race balun with quartz differential line and two interconnects (Fig. 17c). Dashed line: FW simulations. Solid line: measurements.

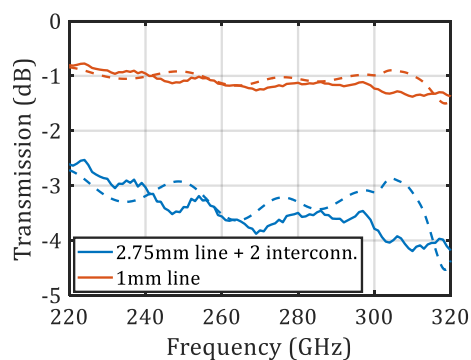


Fig. 19. Transmission for the 2.75 mm transmission line and two interconnects (back-to-back) estimated from the S_{21} measurements in Fig. 18, and calculated transmission for 1mm transmission line. Dashed line: FW simulations. Solid line: measurements.

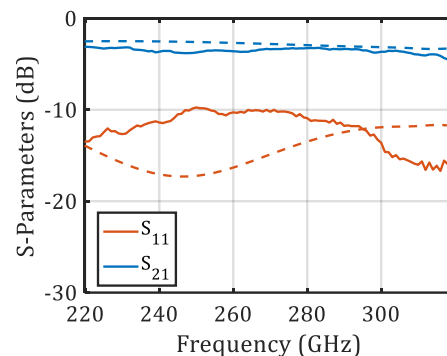


Fig. 20. Delay-line balun S-parameters. Dashed line: FW simulations. Full line: measurements.

REFERENCES

- [1] T. Kürner et al., "Applications Requirement Document (ARD)", DCN: 15-14-0304-16-003d, IEEE 802.15 TG3d, May 2015, <https://mentor.ieee.org/802.15/documents>.
- [2] J. Edstam, J. Hansryd, S. Carpenter, T. Emanuelsson, Y. Li and H. Zirath, Feb. 2017, *Microwave Backhaul Evolution: Reaching Beyond 100 GHz*, Ericsson Technology Review issue 2/2017, Ericsson AB, Stockholm, Sweden.
- [3] K. B. Cooper and G. Chattopadhyay, "Submillimeter-Wave Radar: Solid-State System Design and Applications," *IEEE Microw. Mag.*, vol. 15, no. 7, pp. 51-67, Nov. 2014. doi: 10.1109/MMM.2014.2356092.
- [4] IEEE Standard for High Data Rate Wireless Multi-Media Networks--Amendment 2: 100 Gb/s Wireless Switched Point-to-Point Physical Layer," *IEEE Std 802.15.3d-2017 (Amendment to IEEE Std 802.15.3-2016 as amended by IEEE Std 802.15.3e-2017)*, vol., no., pp.1-55, 18 Oct. 2017. doi: 10.1109/IEEESTD.2017.8066476.
- [5] M. Seo, M. Urteaga, J. Hacker, et al., "InP HBT IC technology for terahertz frequencies: fundamental oscillators up to 0.57 THz," *IEEE J. Solid-State Circuits*, vol. 46, no. 10, pp. 2203-2214, Oct. 2011. doi: 10.1109/JSSC.2011.2163213.
- [6] A. Tessmann, A. Leuther et al., "Metamorphic HEMT MMICs and modules operating between 300 and 500 GHz," *IEEE J. Solid-State Circuits*, vol. 46, no. 10 pp. 2193-2202, Oct. 2011. doi: 10.1109/JSSC.2011.2163212.
- [7] L. Samoska, W. R. Deal, G. Chattopadhyay et al. "A submillimeter-wave HEMT amplifier module with integrated waveguide transitions operating above 300 GHz," *IEEE Trans. Microw. Theory Techn.*, vol. 56, no. 6, pp. 1380-1388, Jun. 2008. doi: 10.1109/TMTT.2008.923353.
- [8] K. M. K. H. Leong, W. R. Deal et al., "A 340-380 GHz integrated CB-CPW-to-waveguide transition for submillimeter-wave MMIC packaging," *IEEE Microw. Wireless Compon. Lett.*, vol. 19, no. 6, pp. 413-415, Jun. 2009. doi: 10.1109/LMWC.2009.2020043.
- [9] A. Tessman et al. "A 243 GHz low-noise amplifier module for use in next-generation direct detection radiometers," *Proc. 2013 European Microwave Integrated Circuit Conf., Nuremberg*, 2013, pp. 220-223.
- [10] M. Alonso-del Pino, C. Jung-Kubiak, T. Reck, C. Lee and G. Chattopadhyay, "Micromachining for Advanced Terahertz: Interconnects and Packaging Techniques at Terahertz Frequencies," *IEEE Microw. Mag.*, vol. 21, no. 1, pp. 18-34, Jan. 2020, doi: 10.1109/MMM.2019.2945157.
- [11] R. Han, Y. Zhang, Y. Kim, D. Y. Kim, H. Shichijo, E. Afshari, and K. K. O., "Active terahertz imaging using Schottky diodes in CMOS: array and 860-GHz pixel," *IEEE J. Solid-State Circuits*, vol. 48, no. 10, pp. 2296-2308, Oct. 2013. doi: 10.1109/JSSC.2013.2269856.
- [12] H. S. Bakshi et al., "Low-Cost packaging of 300 GHz integrated circuits with an on-chip patch antenna," *IEEE Antennas Wireless Propag. Lett.*, vol. 18, no. 11, pp. 2444-2448, Nov. 2019. doi: 10.1109/LAWP.2019.2943371.
- [13] C.-H. Li and T.-Y. Chiu, "340-GHz low-cost and high-gain on-chip higher order mode dielectric resonator antenna for THz applications," *IEEE Trans. THz Sci. Technol.*, vol. 3, no. 7, pp. 284-294, May 2017. doi: 10.1109/TTHZ.2017.2670234.

- [14] X.-D. Deng, Y. Li, C. Liu, W. Wu and Y. -Z. Xiong, "340 GHz on-chip 3-D antenna with 10 dBi gain and 80% radiation efficiency," *IEEE Trans. THz Sci. Technol.*, vol. 5, no. 4, pp. 619–627, July. 2015. doi: 10.1109/TTHZ.2015.2424682.
- [15] X.-D. Deng, Y. Li, W. Wu and Y. -Z. Xiong, "340-GHz SIW cavity-backed magnetic rectangular slot loop antennas and arrays in silicon technology," *IEEE Trans. Antennas Propag.*, vol. 63, no. 12, pp. 5272–5279, Dec. 2015. doi: 10.1109/TAP.2015.2490248.
- [16] X.-D. Deng, Y. Li, H. Tang, W. Wu and Y. -Z. Xiong, "Dielectric loaded endfire antennas using standard silicon technology," *IEEE Trans. Antennas Propag.*, vol. 65, no. 6, pp. 2797–2807, Jun. 2017. doi: 10.1109/TAP.2017.2673800.
- [17] A. J. Alazemi, H. Yang and G. M. Rebeiz, "Double Bow-Tie Slot Antennas for Wideband Millimeter-Wave and Terahertz Applications," *IEEE Trans. THz Sci. Technol.*, vol. 6, no. 5, pp. 682–689, Sept. 2016. doi: 10.1109/TTHZ.2016.2590947.
- [18] S. van Berkel et al., "Wideband Double Leaky Slot Lens Antennas in CMOS Technology at Sub-millimeter Wavelengths," *IEEE Trans. THz Sci. Technol.*, early access. doi: 10.1109/TTHZ.2020.3006750.
- [19] B. Goettel, P. Pahl, C. Kutschker, S. Malz, U. R. Pfeiffer and T. Zwick, "Active multiple feed on-chip antennas with efficient in-antenna power combining operating at 200–320 GHz," *IEEE Trans. Antennas Propag.*, vol. 65, no. 2, pp. 416–423, Feb. 2017. doi: 10.1109/TAP.2016.2634398.
- [20] N. Sarmah, J. Grzyb, K. Statnikov, S. Malz, P. Rodriguez Vazquez, W. Förster, B. Heinemann, and U. R. Pfeiffer, "A fully integrated 240-GHz direct-conversion quadrature transmitter and receiver chipset in SiGe technology," *IEEE Trans. Microw. Theory Techn.*, vol. 64, no. 2, pp. 562–574, Feb. 2016. doi: 10.1109/TMTT.2015.2504930.
- [21] H. Song, J. Kim, K. Ajito, M. Yaita and N. Kukutsu, "Fully Integrated ASK Receiver MMIC for Terahertz Communications at 300 GHz," *IEEE Trans. THz Sci. Technol.*, vol. 3, no. 4, pp. 445–452, July 2013. doi: 10.1109/TTHZ.2013.2252954.
- [22] M. H. Eissa et al., "Wideband 240-GHz Transmitter and Receiver in BiCMOS Technology With 25-Gbit/s Data Rate," *IEEE J. Solid-State Circuits*, vol. 53, no. 9, pp. 2532–2542, Sept. 2018. doi: 10.1109/JSSC.2018.2839037.
- [23] M. Arias Campo, D. Blanco, S. Bruni, A. Neto and N. Llombart, "On the Use of Fly's Eye Lenses with Leaky-Wave Feeds for Wideband Communications," *IEEE Trans. Antennas Propag.*, vol. 68, no. 4, pp. 2480–2493, Apr. 2020. doi: 10.1109/TAP.2019.2952474.
- [24] S. Bosma, M. Alonso-delPino, C. Jung-Kubiak, D. Blanco and N. Llombart, "Scanning Lens Phased Array for Submillimeter Wavelengths," in *Proc. 44th Int. Conf. Infrared, Millimeter, and Terahertz Waves (IRMMW-THz)*, Paris, France, Sep. 2019. doi: 10.1109/IRMMW-THz.2019.8874477.
- [25] N. Llombart, G. Chattopadhyay, A. Skalare, and I. Mehdi, "Novel terahertz antenna based on a silicon lens fed by a leaky wave enhanced waveguide," *IEEE Trans. Antennas Propag.*, vol. 59, no. 6, pp. 2160–2168, Jun. 2011. doi: 10.1109/TAP.2011.2143663.
- [26] S. Beer, H. Gulan, C. Rusch and T. Zwick, "Coplanar 122-GHz Antenna Array With Air Cavity Reflector for Integration in Plastic Packages," *IEEE Antennas Wireless Propag. Lett.*, vol. 11, pp. 160–163, 2012. doi: 10.1109/LAWP.2012.2186783.
- [27] A. Bhutani, B. Göttel, A. Lipp and T. Zwick, "Packaging Solution Based on Low-Temperature Cofired Ceramic Technology for Frequencies Beyond 100 GHz," *IEEE Trans. Compon. Packag. Manuf. Technol.*, vol. 9, no. 5, pp. 945–954, May 2019. doi: 10.1109/TCPMT.2018.2882062.
- [28] N. Chahat, A. Tang, C. Lee, R. Sauleau and G. Chattopadhyay, "Efficient CMOS Systems With Beam-Lead Interconnects for Space Instruments," *IEEE Trans. THz Sci. Technol.*, vol. 5, no. 4, pp. 637–644, Jul. 2015. doi: 10.1109/TTHZ.2015.2446200.
- [29] A. Dyck, M. Rösch, A. Tessmann, A. Leuther, M. Kuri, S. Wagner, B. Gashi, J. Schäfer, and Oliver Ambacher, "A transmitter system-in-package at 300 GHz with an off-chip antenna and GaAs-based MMICs," *IEEE Trans. THz Sci. Technol.*, vol. 9, no. 3, pp. 335–344, May 2019. doi: 10.1109/TTHZ.2019.2910511.
- [30] R. Sauleau, P. Coquet, D. Thouroude, J. - Daniel and T. Matsui, "Radiation characteristics and performance of millimeter-wave horn-fed Gaussian beam antennas," *IEEE Trans. Antennas Propag.*, vol. 51, no. 3, pp. 378–387, March 2003. doi: 10.1109/TAP.2003.809821.
- [31] R. Sauleau, P. Coquet, T. Matsui and J. - Daniel, "A new concept of focusing antennas using plane-parallel Fabry-Perot cavities with nonuniform mirrors," *IEEE Trans. Antennas Propag.*, vol. 51, no. 11, pp. 3171–3175, Nov. 2003. doi: 10.1109/TAP.2003.818795.
- [32] S. A. Hosseini, F. Capolino and F. De Flaviis, "A 44 GHz single-Feed Fabry-Pérot Cavity antenna designed and fabricated on quartz," in *Proc. IEEE Int. Symp. Antennas and Propagation (APS-URSI)*, Spokane, WA, 2011, pp. 1285–1288, doi: 10.1109/APS.2011.5996523.
- [33] D. F. Filipovic, G. P. Gauthier, S. Raman and G. M. Rebeiz, "Off-axis properties of silicon and quartz dielectric lens antennas," *IEEE Trans. Antennas Propag.*, vol. 45, no. 5, pp. 760–766, May 1997. doi: 10.1109/8.575618.
- [34] A. Artemenko, A. Mozharovskiy, A. Maltsev, R. Maslennikov, A. Sevastyanov and V. Ssorin, "Experimental Characterization of E-Band Two-Dimensional Electronically Beam-Steerable Integrated Lens Antennas," *IEEE Antennas Wireless Propag. Lett.*, vol. 12, pp. 1188–1191, 2013. doi: 10.1109/LAWP.2013.2282212.
- [35] W. Shin, B. Ku, O. Inac, Y. Ou and G. M. Rebeiz, "A 108–114 GHz 4x4 Wafer-Scale Phased Array Transmitter With High-Efficiency On-Chip Antennas," *IEEE J. Solid-State Circuits*, vol. 48, no. 9, pp. 2041–2055, Sept. 2013. doi: 10.1109/JSSC.2013.2260097.
- [36] Y. Yang, O. D. Gurbuz and G. M. Rebeiz, "An Eight-Element 370–410-GHz Phased-Array Transmitter in 45-nm CMOS SOI With Peak EIRP of 8–8.5 dBm," *IEEE Trans. Microw. Theory Techn.*, vol. 64, no. 12, pp. 4241–4249, Dec. 2016. doi: 10.1109/TMTT.2016.2613850.
- [37] N. Llombart et al., "Silicon micromachined lens antenna for THz integrated heterodyne arrays," *IEEE Trans. THz Sci. Technol.*, vol. 3, no. 5, pp. 515–523, Sep. 2013. doi: 10.1109/TTHZ.2013.2270300.
- [38] D. R. Jackson, A. A. Oliner, "A Leaky-wave analysis of the high-gain printed antenna configuration," *IEEE Trans. Antennas Propag.*, vol. 36, no. 7, pp. 905–910, Jul. 1988. doi: 10.1109/8.7194.
- [39] F. Scattone, M. Ettore, B. Eddo, R. Sauleau and N. J. G. Fonseca, "Truncated Leaky-Wave Antenna With Coscant-Squared Radiation Pattern," *IEEE Antennas Wireless Propag. Lett.*, vol. 17, no. 5, pp. 841–844, May 2018. doi: 10.1109/LAWP.2018.2818668.
- [40] D. Jackson, A. Oliner, and A. Ip, "Leaky-wave propagation and radiation for a narrow-beam multiple-layer dielectric structure," *IEEE Trans. Antennas Propag.*, vol. 41, no. 3, pp. 344–348, Mar. 1993. doi: 10.1109/8.233128.
- [41] D. Blanco, E. Rajo-Iglesias, S. Maci, and N. Llombart, "Directivity Enhancement and Spurious Radiation Suppression in Leaky-Wave Antennas Using Inductive Grid Metasurfaces," *IEEE Trans. Antennas Propag.*, vol. 63, no. 3, pp. 891–900, Mar. 2015. doi: 10.1109/TAP.2014.2387422.
- [42] A. Neto, N. Llombart, G. Gerini, M. D. Bonnedal and P. de Maagt, "EBG enhanced feeds for the improvement of the aperture efficiency of reflector antennas," *IEEE Trans. Antennas Propag.*, vol. 55, no. 8, pp. 2185–2193, Aug. 2007. doi: 10.1109/TAP.2007.901854.
- [43] M. Kominami, D. M. Pozar, and D. H. Schaubert, "Dipole and slot elements and arrays on semi-infinite substrates," *IEEE Trans. Antennas Propag.*, vol. AP-33, no. 6, pp. 600–607, June 1985. doi: 10.1109/TAP.1985.1143638.
- [44] A. Polemi and S. Maci, "On the Polarization Properties of a Dielectric Leaky Wave Antenna," *IEEE Antennas Wireless Propag. Lett.*, vol. 5, pp. 306–310, Jul. 2006. doi: 10.1109/LAWP.2006.878889.
- [45] D. R. Jackson and A. A. Oliner, "Leaky-wave antennas," in *Modern Antenna Handbook*, C. Balanis, Ed. New York: Wiley, 2008, ch. 7, pp. 325–367.
- [46] EMPIRE XPU, Available "http://www.empire.de".
- [47] S. Sahin, N. K. Nahar, and K. Sertel, "Thin-film SUEX as an antireflection coating for mmW and THz applications," *IEEE Trans. THz Sci. and Technol.*, vol. 9, no. 4, pp. 417–421, Jul. 2019. doi: 10.1109/TTHZ.2019.2915672.
- [48] M. Arias Campo, G. Carluccio, D. Blanco, O. Litschke, S. Bruni, and N. Llombart, "Wideband circularly polarized antenna with in-lens polarizer for high-speed communications," *IEEE Trans. Antennas Propag.*, accepted for publication.
- [49] M. Spirito, G. Gentile and A. Akhnouk, "Multimode analysis of transmission lines and substrates for (sub)mm-wave calibration," *82nd ARFTG Microwave Measurement Conf.*, Columbus, OH, United States, Nov. 2013, pp. 1–6. doi: 10.1109/ARFTG-2.2013.6737356.



Marta Arias Campo received the M.Sc. degree in telecommunications engineering from the Universidad Politécnica de Madrid, Madrid, Spain, in 2009. She is currently pursuing the Ph.D. degree in the Terahertz Sensing Group, Technical University of Delft, Delft, The Netherlands, in collaboration with IMST GmbH, Kamp-Lintfort, Germany.

In 2009, she joined the Antennas and EM Modeling Department, IMST GmbH, where she currently works as a Research and Development Antenna Engineer in the Antenna Front-ends Team, with the main focus on the design of active planar antenna arrays. In 2016, she joined the Terahertz Sensing Group, Technical University of Delft, Delft, The Netherlands. Her research interests include the analysis and design of lens antennas and quasi-optical structures for high-speed wireless communications and radar applications.

Katarzyna Holc received the M.Sc. degree in physics from Warsaw University, Warsaw, Poland, with specialization in optics and focus on femtosecond laser systems in 2003. Following her interest in lasers, she joined the Institute of High Pressure Physics, Polish Academy of Sciences in Warsaw, working on GaN-based blue laser diodes. After obtaining her Ph.D. in 2011, she moved to Freiburg, Germany, to join the Technology Department, Fraunhofer Institute for Applied Solid State Physics IAF, to work on technology development dedicated to III-V semiconductor devices.



Rainer Weber was born in Offenburg, Germany, in 1978. He received the Dipl.-Ing. degree in electrical engineering from the University of Applied Sciences, Offenburg, Germany, in 2003. He then joined the High Frequency Devices and Circuits Department, Fraunhofer-Institute for Applied Solid State Physics, Freiburg, Germany, where he is involved with the MMIC design of amplifiers, oscillators, multipliers, and mixers up to 600 GHz.



Carmine De Martino was born in Salerno, Italy, in 1988. He received the master's degrees in electrical engineering from the University of Naples "Federico II", Naples, Italy, in 2015. He is currently pursuing the Ph.D. degree at the Delft University of Technology, Delft, The Netherlands. In 2015, he joined the Electronic Research Laboratory Group, Delft University of Technology, as a Researcher. His research interests include the development of

new paradigms in calibration and measurement techniques until the sub-THz frequency range, small- and large-signal devices' characterization, 3-D electromagnetic simulations of passive structures, and antenna characterization in mm-Wave and sub-THz frequency range. Mr. De Martino was a recipient of the Best Student Paper Award for his contribution at the 2019 93rd ARFTG Microwave Measurement Conference (ARFTG).



Marco Spirito received the M.Sc. degree (cum laude) in electrical engineering from the University of Naples "Federico II," Naples, Italy, in 2000, and the Ph.D. degree from the Delft University of Technology, Delft, The Netherlands, in 2006.

From 2000 to 2001, he was a Guest Researcher with Infineon Technologies, Munich, Germany. In 2006, he joined the Department of Electronics and Telecommunications Engineering, University of Naples "Federico II." In April 2008, he joined the Electronics Research Laboratory, Delft University of Technology, as an Assistant Professor, where he has been an Associate Professor since April 2013. In 2010 and 2017, he was one of the co-founders of Anteverta-mw B.V., Eindhoven, The Netherlands, and Vertigo Technologies B.V., Delft, respectively, two companies pioneering innovative measurement techniques and instruments. His research interests include the development of advanced

passive components and building blocks operating in the millimeter and submillimeter frequency ranges, the development of characterization setups and calibration techniques for millimeter and submillimeter waves, and the design and integration of mm-wave sensing systems.

Dr. Spirito was a recipient of the Best Student Paper Award for his contribution to the 2002 IEEE Bipolar/BiCMOS Circuits and Technology Meeting (BCTM). He received the IEEE MTT Society Microwave Prize in 2008. He was a co-recipient of the Best Student Paper Award at the IEEE Radio Frequency Integrated Circuits Symposium (RFIC) 2011, the GAAS Association Student Fellowship in 2012, the Best Student Paper Award in second place at the International Microwave Biomedical Conference (IMBioC) 2018, the Best Paper Award at the 2019 Winter ARFTG Microwave Measurement Conference (ARFTG) Conference, and the Best Student Paper Award at the 2019 Summer ARFTG Conference.



Arnulf Leather received the Dipl.Phys. and Ph.D. degrees in physics from the Technical University of Aachen, Aachen, Germany.

He is with the Fraunhofer Institute for Applied Solid State Physics (IAF) since 1996. The major working area is the development of HEMT technologies for sensor and communication systems up to 600 GHz.



Simona Bruni received the Laurea degree in telecommunication engineering and the Ph.D. degree in electromagnetics from the University of Siena, Siena, Italy, in 2002 and 2006, respectively. Her Ph.D. degree was financed and hosted by the Defense, Security and Safety Institute of the Netherlands Organization for Applied Scientific Research (TNO), The Hague, The Netherlands.

She worked as a Researcher with the Defense, Security and Safety Institute of the Netherlands Organization for Applied Scientific Research (TNO). From 2007 to 2013, she worked as an Research and Development Antenna Engineer with the Calcareo Advanced Technology (CAT) Department, Calcareo SPA, Vicenza, Italy. Since 2013, she has been with the Antennas and EM Modeling Group, IMST GmbH, Kamp-Lintfort, Germany, where she works as a Research and Development Antenna Engineer with the Antenna Front-Ends Team. Her research interests include the design of integrated antennas, high-frequency antenna arrays, and front-end design for communications and automotive applications.



Nuria Llombart received the master's degree in electrical engineering and the Ph.D. degree from the Polytechnic University of Valencia, Valencia, Spain, in 2002 and 2006, respectively. During her master's degree, she spent 1 year with the Friedrich-Alexander University of Erlangen-Nuremberg, Erlangen, Germany.

She worked with the Fraunhofer Institute for Integrated Circuits, Erlangen. From 2002 to 2007, she was with the Antenna Group, TNO Defense, Security and Safety Institute, The Hague, The Netherlands, where she was working as a Ph.D. Student and then as a Researcher. From 2007 to 2010, she was a Post-Doctoral Fellow with the California Institute of Technology, working with the Submillimeter Wave Advance Technology Group, Jet Propulsion Laboratory, Pasadena, CA, USA. She was a Ramón y Cajal Fellow with the Optics Department, Complutense University of Madrid, Madrid, Spain, from 2010 to 2012. In September 2012, she joined the THz Sensing Group, Technical University of Delft, Delft, The Netherlands, where she became a Full Professor in 2018. She has co-authored more than 150 journals and international conference contributions. Her research interests include the analysis and design of planar antennas, periodic structures, reflector antennas, lens antennas, and waveguide structures, with emphasis in the terahertz range.

Dr. Llombart was a recipient of the H. A. Wheeler Award for the Best Applications Paper of 2008 in the IEEE Transactions on Antennas and Propagation, the 2014 THz Science and Technology Best Paper Award of the IEEE Microwave Theory and Techniques Society, and several NASA awards.

She was also a recipient of the 2014 IEEE Antenna and Propagation Society Lot Shafai Mid-Career Distinguished Achievement Award. She serves as a Board Member for the IRMMW-THz International Society. In 2015, she was a recipient of European Research Council Starting Grant.